

Graph-Based Intercategory and Intermodality Network for Multilabel Classification and Melanoma Diagnosis of Skin Lesions in Dermoscopy and Clinical Images

Xiaohang Fu, Lei Bi, Ashnil Kumar, Michael Fulham, and Jinman Kim

X. Fu, L. Bi, M. Fulham, and J. Kim are with the School of Computer Science, Faculty of Engineering, The University of Sydney, NSW 2006, Australia (e-mail: xiaohang.fu@sydney.edu.au, lei.bi@sydney.edu.au, michael.fulham@sydney.edu.au, and jinman.kim@sydney.edu.au). M. Fulham is also with the Department of Molecular Imaging, Royal Prince Alfred Hospital. A. Kumar is with the School of Biomedical Engineering, Faculty of Engineering, The University of Sydney, NSW 2006, Australia (email: ashnil.kumar@sydney.edu.au). Corresponding authors: Xiaohang Fu and Jinman Kim.

Abstract

The identification of melanoma involves an integrated analysis of skin lesion images acquired using the clinical and dermoscopy modalities. Dermoscopic images provide a detailed view of the subsurface visual structures that supplement the macroscopic clinical images. Melanoma diagnosis is commonly based on the 7-point visual category checklist (7PC). The 7PC contains intrinsic relationships between categories that can aid classification, such as shared features, correlations, and the contributions of categories towards diagnosis. Manual classification is subjective and prone to intra- and interobserver variability. This presents an opportunity for automated methods to improve diagnosis. Current state-of-the-art methods focus on a single image modality and ignore information from the other, or do not fully leverage the complementary information from both modalities. Further, there is not a method to exploit the ‘intercategory’ relationships in the 7PC. In this study, we address these issues by proposing a graph-based intercategory and intermodality network (GIIN) with two modules. A graph-based relational module (GRM) leverages intercategorical relations, intermodal relations, and prioritises the visual structure details from dermoscopy by encoding category representations in a graph network. The category embedding learning module (CELM) captures representations that are specialised for each category and support the GRM. We show that our modules are effective at enhancing classification performance using a public dataset of dermoscopy-clinical images, and show that our method outperforms the state-of-the-art at classifying the 7PC categories and diagnosis.

Index Terms—Melanoma, Classification, Dermoscopy, Multimodal Image

1. Introduction

Melanoma is the deadliest form of skin cancer [1, 2]. It had the fastest rate of incidence increase over the last 50 years compared to all other cancers, with the highest incidence in Australia and New Zealand [1]. Early diagnosis is critical as early stage melanoma is curable [3]. Clinical diagnosis involves a visual assessment of a skin lesion and its appearance is then classified. The skin lesion is first examined with the naked eye and clinical photography with a digital camera, and then by dermoscopy [4]. Clinical images capture a macroscopic view showing the colour and geometry of lesions, but they cannot depict subsurface details such as ‘dots’ and ‘globules’. They are also less standardised and there may be large variations in the field-of-view and lighting, and the skin may have tattoos or body piercings. Dermoscopy is more advanced and provides a more comprehensive examination of the lesion, and has been proven to improve the accuracy of melanoma diagnosis [5-8]. Dermoscopy provides a magnified (typically 10×) microscopic view of the lesion by covering the lesion in fluid or using cross-polarised light filters to eliminate surface reflection. This reveals further subsurface structures which cannot be seen on clinical images, including dots, globules, and vascularity, thereby providing valuable visual information. Integrated clinical and dermoscopy examinations are now routine in clinical practice [9]. Examples of clinical and dermoscopic image pairs of skin lesion cases with category classifications are presented in Fig. 1.

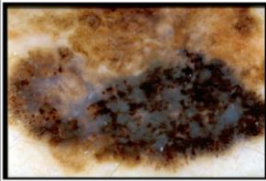

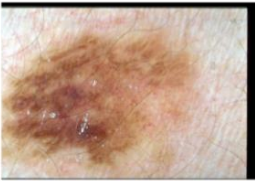
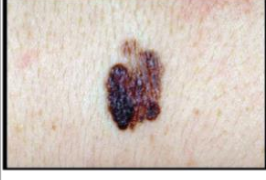


	a)	b)	c)
Dermoscopy Image			
Clinical Image			
Diagnosis (DIAG)	Melanoma	Reed or Spitz Nevus	Clark Nevus
Pigment Network (PN)	Atypical	Atypical	Absent
Streaks (STR)	Irregular	Irregular	Irregular
Pigmentation (PIG)	Diffuse Irregular	Absent	Absent
Regression Structures (RS)	Combinations	Absent	Absent
Dots and Globules (DaG)	Irregular	Irregular	Regular
Blue Whitish Veil (BWV)	Present	Present	Absent
Vascular Structures (VS)	Absent	Dotted	Dotted

Fig. 1. Three examples of skin lesions (melanoma, spitz nevus, and clark nevus) showing their appearance on dermoscopic and clinical images, and their category classifications.

The 7-point checklist (7PC) is a reliable and one of the most common diagnostic approaches for melanoma [4, 8, 10]. The method involves simultaneously assessing seven visual characteristics of the lesion: pigment network (PN), streaks (STR), pigmentation (PIG), regression structures (RS), dots and globules (DaG), blue whitish veil (BWV), and vascular structures (VS). Each category contributes to a score if its classification is indicative of melanoma, and the lesion is suspected of being a melanoma if the total score is ≥ 3 [11]. However, classification of the 7PC is a complex and subjective task as many characteristics are simultaneously assessed, and the expressions of each category can vary (e.g., compare examples of the same class in Fig. 1). This can lead to high intra- and interobserver variations and misdiagnosis [12]. Diagnostic accuracy is also highly dependent on the experience of the examiner [6], and dermoscopic assessment can be difficult to learn [13]. An automated method may improve diagnosis, eliminate subjective evaluation, and be adopted for mass screening.

Early automated methods classified melanoma by first detecting the lesion border, extracting multiple handcrafted features of the lesion relating to shape, texture, and colour, then applied classifiers such as support vector machines (SVMs) [14-19]. Celebi et al. [15] used feature selection algorithms to determine an optimal set of features. Fabbrocini et al. [16] constructed specialised image processing pipelines for each category of the 7PC. However, these handcrafted feature-based methods are heavily dependent on image pre-processing and require specialist knowledge to compute the visual descriptors of each category.

More recently, convolutional neural networks (CNNs) have been successful across numerous image-related problems and have been applied to classify skin lesions. Previous efforts have been typically limited to a single modality (most commonly dermoscopy) and directly predicted melanoma diagnosis [20-24]. Progress in this field has been stimulated by the recurring International Skin Imaging Collaboration's skin lesion classification challenge [25, 26]. The high-performing methods in the challenge showed superior accuracy compared to dermatologists for the classification of melanoma. Yu et al. [21] segmented the lesions using a fully convolutional residual network then performed melanoma classification on cropped lesions. Gessert et al. [24] combined meta-data with dermoscopic images and ensembled multi-resolution CNNs. These methods, however, were designed for single image modality inputs.

Multimodal methods for dual clinical and dermoscopy modalities are rarer. Such an approach must address the optimal use of complementary features in the input image pair, account for the value of each image type for different categories, and assimilate the information to improve classification. A simple strategy has been late fusion, in which features are extracted

separately from each modality, then concatenated together in the later stages of the model [11, 27, 28]. Kawahara et al. [11] performed multiclass skin lesion classification by concatenating different combinations of features extracted from dermoscopic and clinical images by a pre-trained Inception network with the patient's meta-data (such as patient gender and lesion location). The use of concatenation to combine features from different modalities, however, disregards the relative merits of each modality in classification. Bi et al. [29] reported a hyper-connected CNN (HcCNN), which incorporated a hyper-branch to assimilate features from both modalities at different scales to classify the 7PC and diagnosis. Although this approach was more effective at combining multimodal features, as with other methods, it did not encode the relative advantages of each modality or fully leverage complementary features. Previous methods also ignored the intrinsic relationships within the 7PC, including the direct contributions of the 7PC categories toward diagnosis. We suggest that correlations between the presence or absence of different categories, and the exchange of mutual features between the categories will be valuable to improve classification performance.

Recently, graph neural networks (GNNs) have garnered considerable interest and have proven powerful in a range of applications, including its ability to represent relationships between attributes [30]. GNNs model objects as nodes and capture their relations as edges, and therefore can represent a large variety of data types including non-Euclidean data. Graph convolutional networks (GCNs) [31] extend GNNs by performing convolutions on neighbouring node features. Rather than assume that each neighbour should contribute equally towards the central node, Veličković et al. [32] introduced the graph attention network (GAT) to adaptively assign coefficients for each neighbour. GCNs have been employed to model relations between labels in multilabel image classification problems. Chen et al. [33] modelled interdependencies among the labels as a GCN using word embeddings and combined it with a CNN backbone that extracted visual features. Other frameworks of a similar architecture have been explored for multilabel image-based problems [34-38]. Hou et al. [37] combined CNN features of chest X-ray images with disease label embeddings using a transformer encoder, then employed a GCN for visual-semantic learning and multilabel disease classification. Wu et al. [38] used a GCN to characterise the co-occurrence of skin conditions for their classification in clinical images. These existing GCN-based methods, however, are not suitable for multimodal images, as they cannot optimally assimilate the visual characteristics unique to each modality.

1.1. Our Contributions

In this study, we propose a graph-based intercategory and intermodality network (GIIN) for melanoma classification where we leverage the inherent relationships between visual characteristics that correspond to the 7PC, and complementary information from clinical and dermoscopy images. We leverage this in a manner that prioritises the information from dermoscopy. Our contributions to the state-of-the-art are as follows:

- We propose a graph-based relational module (GRM) to exploit intercategory relationships. The GRM represents the categories as a set of two star graphs, each corresponding to the dermoscopic or clinical image modality, and is composed of a central diagnosis node with 7 leaves. This topology encodes the relationships between diagnosis and the other 7 categories, and the relationships between the 7 categories.
- The GRM includes directional edges between corresponding nodes of the same category in the dermoscopic and clinical star graphs to use complementary visual features from both modalities. These single directional edges (from dermoscopy to clinical) prioritise the dermoscopy features and allow the intermodal relationships to self-adapt independently for each category.
- We also propose a category embedding learning module (CELM) to automatically transform general CNN features of the skin lesion from the image pair into embedded representations that are meaningful and specialised to each of the categories. These transformed features are designed to support the relational learning downstream.

We outline these contributions in our overview of the methods in Fig. 2.

2. Methodology

2.1. Materials

We used the publicly available 7PC dataset [11], which is comprised of dermoscopic and clinical image pairs from 1,011 patients. The authors split the dataset into 413 training, 203 validation, and 395 test studies. The size ($h \times w$) of the dermoscopic images ranged from 474×512 to 532×768 pixels, and the clinical images ranged from 480×512 to 532×768 pixels. There were 8 categories – 7 from the 7PC and diagnosis (DIAG). DIAG had 5 different

classes: basal cell carcinoma (BCC), nevus (NEV), melanoma (MEL), miscellaneous (MISC), and seborrheic keratosis (SK). The classes of the other categories included: i) absent (ABS), ii) typical (TYP), iii) regular (REG), iv) present (PRS), v) atypical (ATP), and vi) irregular (IR). Classes (iv) to (vi) contribute to the 7-point score. For a full breakdown of the categories including the number of examples of each class, please refer to the original paper of the dataset [11].

2.2. Graph-Based Intercategory and Intermodality Network (GIIN)

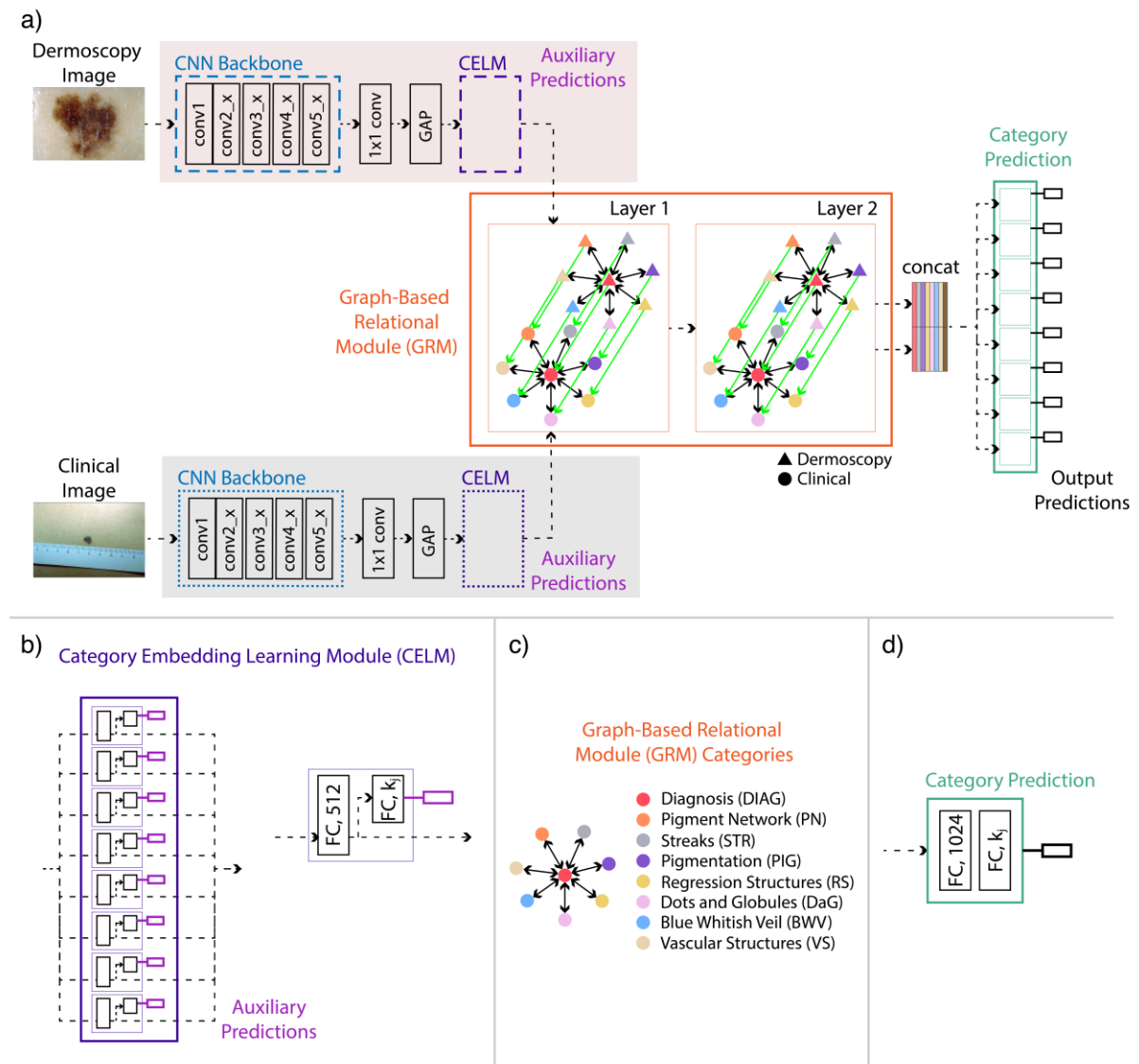


Fig. 2. Overview of our proposed approach: a) the GIIN with CELM and GRM, b) CELM with a detailed isolated unit for a single category, c) star structure of GRM for one modality in which the 7PC categories are connected to the central node of diagnosis, and d) a unit of category prediction component.

In our method, information from each modality is first extracted and processed in unique branches by separate CNN backbones and CELMs, then amalgamated in the GRM. The

outputs of the GRM are used to predict the 7PC. We use the ResNet-50 model as the CNN backbone for visual feature extraction due to its versatility across a range of image-based problems including skin lesion analysis [20, 22, 27, 29]. Our method can support other backbones and we later show that the CELM and GRM can enhance the performance of various backbone CNNs. We inserted a 1×1 convolution layer immediately after the ‘conv5_x’ block of the backbone to reduce the number of feature channels from 2,048 to 512 for each branch. This further reduces the number of parameters downstream in the model and minimises the risk of overfitting. The feature volumes are subsequently vectorised by global average pooling (GAP) layers, producing vectors of $\mathbf{x}^{\mathbf{g},\mathbf{D}} \in \mathbb{R}^{1 \times 1 \times 512}$ for dermoscopic images and $\mathbf{x}^{\mathbf{g},\mathbf{C}} \in \mathbb{R}^{1 \times 1 \times 512}$ for clinical images.

2.3. Category Embedding Learning Module (CELM)

Prior to relational learning, the extracted visual information is transformed into latent feature vectors that are specialised for each category by the CELM. There are eight units in the CELM of each modality, corresponding to the 7PC categories. We define the units to output classification predictions as:

$$\mathbf{f}_{\text{CELM},j}^{\mathbf{D}}(\mathbf{x}^{\mathbf{g},\mathbf{D}}) = \mathbf{W}_{0,j}^{\mathbf{D}}\mathbf{x}^{\mathbf{g},\mathbf{D}} + \mathbf{b}_{0,j}^{\mathbf{D}} \quad \mathbf{f}_{\text{CELM},j}^{\mathbf{C}}(\mathbf{x}^{\mathbf{g},\mathbf{C}}) = \mathbf{W}_{0,j}^{\mathbf{C}}\mathbf{x}^{\mathbf{g},\mathbf{C}} + \mathbf{b}_{0,j}^{\mathbf{C}} \quad (1)$$

$$\mathbf{p}_{\text{CELM},j}^{\mathbf{D}}(\mathbf{f}_{\text{CELM},j}^{\mathbf{D}}) = \sigma(\mathbf{W}_{1,j}^{\mathbf{D}}\mathbf{f}_{\text{CELM},j}^{\mathbf{D}} + \mathbf{b}_{1,j}^{\mathbf{D}}) \quad \mathbf{p}_{\text{CELM},j}^{\mathbf{C}}(\mathbf{f}_{\text{CELM},j}^{\mathbf{C}}) = \sigma(\mathbf{W}_{1,j}^{\mathbf{C}}\mathbf{f}_{\text{CELM},j}^{\mathbf{C}} + \mathbf{b}_{1,j}^{\mathbf{C}}) \quad (2)$$

where $\mathbf{p}_{\text{CELM},j} \in \mathbb{R}^{1 \times k}$ denotes the predicted class probabilities of category j with k classes, σ is softmax activation, and $\mathbf{f}_{\text{CELM},j} \in \mathbb{R}^{512 \times 1}$ is the intermediate CELM feature vector. The CELM unit of a category is characterised by a set of trainable weights and biases of two fully connected layers, comprising of $\mathbf{W}_0 \in \mathbb{R}^{512 \times 512}$, $\mathbf{W}_1 \in \mathbb{R}^{512 \times 1}$, $\mathbf{b}_0 \in \mathbb{R}^{512 \times 1}$, and $\mathbf{b}_1 \in \mathbb{R}^{1 \times 1}$.

The predictions are used to compute the auxiliary cross-entropy losses for each category and modality that contribute towards the total training loss (details in Section 2.5). Hence, CELM ensures that $\mathbf{f}_{\text{CELM}}^{\mathbf{D}}$ and $\mathbf{f}_{\text{CELM}}^{\mathbf{C}}$ are meaningful for each of the categories prior to the relational processing of the categories in the GRM. The auxiliary predictions are only used during model training and have no role at inference time.

2.4. Graph-Based Relational Module (GRM)

The GRM is comprised of two GNN layers with the same graph topologies. Relations between categories are modelled with a star-shaped graph that reflects the inherent associations of the 7PC, consisting of a central diagnosis node that is connected to all other categories via bidirectional (inverse) edges. There are two star-shaped structures in each GNN layer, corresponding to the two modalities. Directed edges propagate information from the dermoscopy to clinical modality.

The input feature vector for the node of category j is $\mathbf{f}_{\text{CELM},j}^{\text{D}}$ for dermoscopy or $\mathbf{f}_{\text{CELM},j}^{\text{C}}$ for clinical. In GCNs, each node receives the aggregated features of its neighbourhood and a non-linear activation function is applied on the output. Multiple GCN layers can be stacked to learn higher order representations and allow each node to receive information from more distant nodes (more ‘hops’) as shown in Fig. 3. In a standard GCN, the neighbouring nodes are weighted equally towards the central node. We used the GAT [32] approach to assign different contributions for each neighbour.

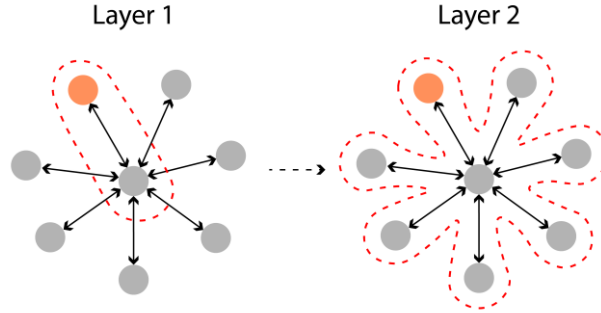


Fig. 3. GCN layers are stacked so that each node receives information from other connected nodes that are a larger number of hops (distance between the nodes) away.

2.4.1. Graph Attention Networks (GATs)

The graph attentional layer computes normalised attention coefficients via a self-attention mechanism:

$$\alpha_{uv} = \frac{\exp(\text{LeakyReLU}(\mathbf{a}^T[\mathbf{W}\mathbf{h}_u \parallel \mathbf{W}\mathbf{h}_v]))}{\sum_{k \in \mathcal{N}_u} \exp(\text{LeakyReLU}(\mathbf{a}^T[\mathbf{W}\mathbf{h}_u \parallel \mathbf{W}\mathbf{h}_k]))} \quad (3)$$

where $\mathbf{h} = \{\mathbf{h}_1, \mathbf{h}_2, \dots, \mathbf{h}_N\}$, $\mathbf{h}_i \in \mathbb{R}^F$ represents the input feature vectors to the GAT layer with $N = 16$, corresponding to the eight categories of the two modalities, α_{uv} is the attention coefficient for node v to u , and \mathcal{N}_u denotes the neighbourhood nodes of u . The feature vectors are linearly transformed via $\mathbf{W} \in \mathbb{R}^{F' \times F}$, the weight matrix shared for every node, then by

$\mathbf{a} \in \mathbb{R}^{2F'}$, the weight vector of a single-layer feedforward neural network of the attention mechanism, with \parallel representing concatenation. LeakyReLU nonlinearity (with a slope of 0.2 for inputs < 0) followed by softmax normalisation are then applied.

The updated feature vectors, $\mathbf{h}' = \{\mathbf{h}'_1, \mathbf{h}'_2, \dots, \mathbf{h}'_N\}$, $\mathbf{h}'_i \in \mathbb{R}^{F'}$, can then be computed by proportionally aggregating over neighbouring nodes:

$$\mathbf{h}'_u = \sigma \left(\sum_{v \in \mathcal{N}_u} \alpha_{uv} \mathbf{W} \mathbf{h}_v \right) \quad (4)$$

where σ is the exponential linear unit (ELU) nonlinearity [39].

Furthermore, we used the multi-head attention mechanism for better stability, computing multiple independent attention coefficients for each node that are aggregated via concatenation:

$$\mathbf{h}'_u = \parallel_{m=1}^M \sigma \left(\sum_{v \in \mathcal{N}_u} \alpha_{uv}^m \mathbf{W}^m \mathbf{h}_v \right) \quad (5)$$

where, for the m -th attention head, α_{uv}^m are the normalised attention coefficients and \mathbf{W}^m are the weights of the input linear transformation. In the first layer, we use 8 attention heads per node and $F_0 = 8$, thereby computing a total of 64 features, as done in the original paper [32]. For the second layer, we compute $F_1 = 512$ features with a single attention head.

2.5. Category Classification and Training

After the GRM layers, the node vectors for each category from the two modalities are concatenated together, yielding eight vectors. These vectors are fed through the final category prediction units, each of which comprise two more fully connected layers and softmax activation to output class probabilities. The model is trained by minimising the total cross-entropy loss between the prediction and ground truth classes, and the auxiliary losses from the CELM of both modalities:

$$\arg \min_{\theta} \sum_{i=1}^M \sum_{j=1}^N L^P(d^i, c^i; y_j^{P,i}, y_j^i) \quad (6)$$

$$L^{total} = \lambda_D L^{CELM,D} + \lambda_C L^{CELM,C} + L^P \quad (7)$$

where $y_j^{P,i}$ and y_j^i denote the final prediction and ground truth for category j of case i , L^P is the cross-entropy loss between the final predictions and ground truth, d is the dermoscopic image, c the clinical image, and θ represent the model parameters. The total training loss comprises of

L^P and the CELM auxiliary losses, $L^{CELM,D}$ and $L^{CELM,C}$, which are balanced against L^P with λ_D and λ_C .

2.6. Implementation Details

The following implementation and hyperparameter choices were kept consistent for all experiments to ensure that there was a fair comparison. The networks were trained end-to-end from scratch for 100 epochs using stochastic gradient descent with a batch size of 4. We employed the Adam optimiser [40] to minimise the mean multi-task cross-entropy loss at a fixed learning rate of 0.00001, with a first moment estimate of 0.9 and second moment estimate of 0.999. We set the weights of the auxiliary losses, λ_D and λ_C , to both be 0.5, as determined empirically (evaluation in Supplementary Materials Table S1). The weights of the backbone were initialised using the ResNet-50 model that was pre-trained on ImageNet [41], then further trained with the rest of our model. This approach has been commonly adopted in previous skin lesion studies to overcome the limitations of using a small training set [11, 20, 21, 24, 29]. Weights of the 1×1 convolutional layers were initialised using He et al.’s method [42] while biases were initialised to zero. Glorot (Xavier) initialisation [43] was used for fully connected layers. Dropout was not used in any experiment.

Each image was mean-subtracted and normalised to unit variance using the training set mean and standard deviation of its image type (dermoscopy or clinical). We employed standard online (on-the-fly) image data augmentation by randomly applying a flip (horizontal or vertical), rotation (of 90, 180 or 270 degrees), random crop, or adding Gaussian noise to the input images. All images were resized to 512×768 pixels with bilinear interpolation, to match the size of the largest images in the dataset. The order of training examples was shuffled for every epoch. All networks were implemented using the PyTorch framework [44]. Both training and testing were performed with a 12GB NVIDIA GTX Titan V GPU. Training required about 4 hours for completion.

2.7. Evaluation Setup

Our performance metrics were: the commonly used area under receiver operating characteristic curve (AUC), sensitivity (Sens), specificity (Spec), and precision (Prec). For AUC, we followed the one-against-all approach as adopted by comparison studies [11, 29].

2.7.1. Ablation Study

We performed an ablation study to determine the contributions from each module. The baseline was the version of our GIIN without CELM and GRM. We then evaluated the effectiveness of CELM by incorporating it into the branches of each modality. We assessed the performance of several topological variants of GRM (Fig. 4) to verify that intermodality connections directed from the dermoscopy to the clinical modalities (GRM-DC) delivered the best performance. We compared this against: i) using separate graphs for each modality without intermodal edges (GRM-Separate), ii) pre-concatenation of the feature vectors for each modality that effectively fused the GRM into a single modality graph (GRM-Fused), iii) using inverse intermodality edges between the modalities (GRM-INV), or iv) directed from the clinical to dermoscopy modalities (GRM-CD). A simple concatenation of feature vectors from both modalities without GRM was applied for the baseline without CELM and GRM, and for the version that only had CELM. Additionally, we compared the performance of our GIIN on melanoma diagnosis against training only on melanoma diagnosis without the other categories and without our modules. For this approach we concatenated the features extracted from the two modalities.

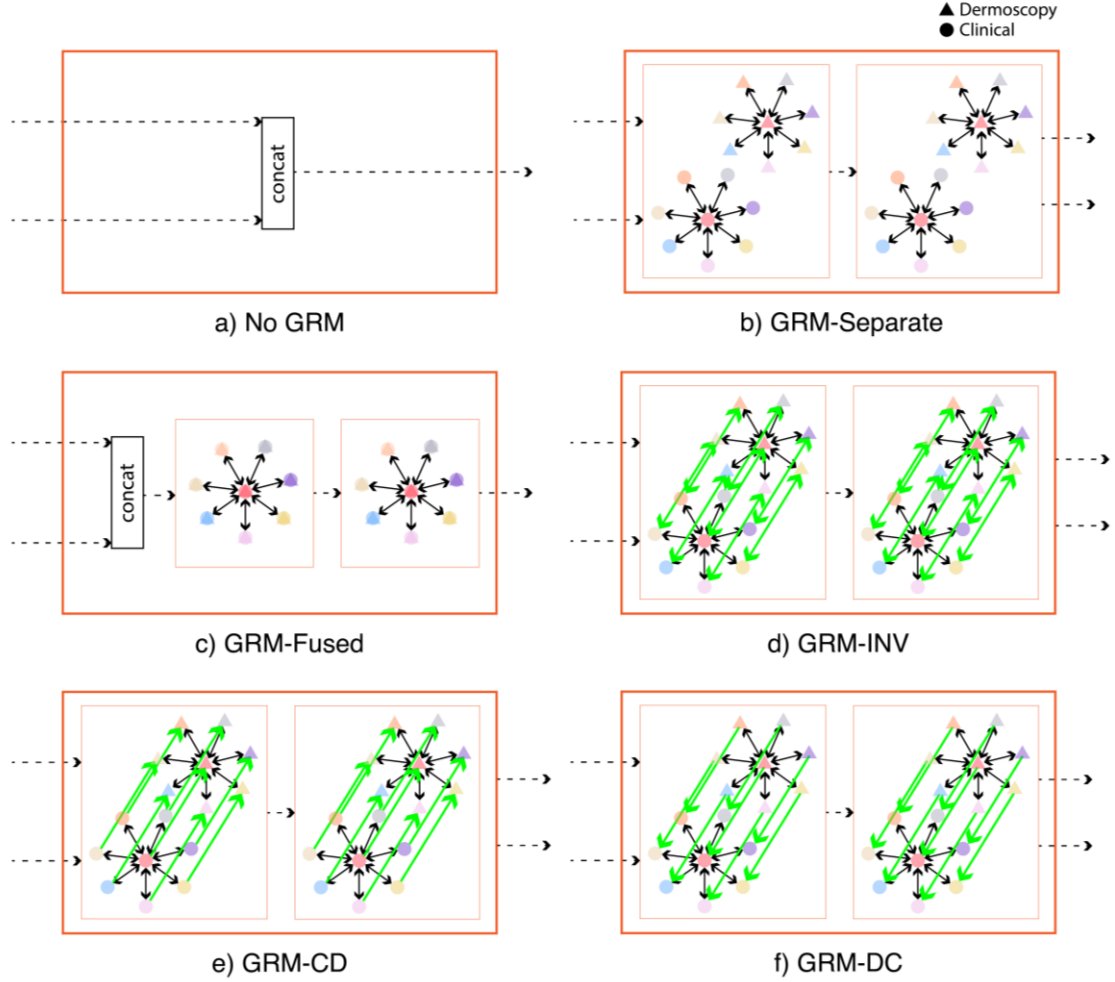


Fig. 4. Different approaches to assimilate multimodal features using a) a simple concatenation without GRM; or variations of our GRM involving b) separate disconnected graphs for each modality; c) pre-concatenation of the feature vectors for each modality; or intermodality edges directed d) inversely between the modalities, e) from clinical to dermoscopy, or f) dermoscopy to clinical (proposed).

2.7.2. Comparison to the State-of-the-Art

We benchmarked the proposed GIIN against the state-of-the-art methods of Kawahara et al. [11] and Bi et al. [29] using the same dataset. The method of Kawahara et al. included three different approaches: Inception-unbalanced (no class balancing sampling strategy during training), Inception-balanced (class balancing during training to counter the imbalanced class distributions in the dataset), and Inception-combined (averaging predicted probabilities of layers that used i) dermoscopic images, ii) dermoscopy and meta-data, or iii) dermoscopy, clinical, and meta-data). The method of Bi et al. [29] was the hyper-connected CNN (HcCNN) which added a multimodal branch to combine and process information from the dermoscopy and clinical branches. HcCNN also used ResNet-50 as the feature extractor backbone for each modality.

2.7.3. Application to Different Backbones

We also investigated the applicability of our proposed CELM and GRM to other feature extractor backbones, including MobileNetV2 [45], ResNet-18, and ResNet-34 [46], by swapping out the ResNet-50 backbone. The final output classification layers of each backbone were discarded as they served no purpose. All these alternatives were pre-trained on ImageNet and fine-tuned with the rest of our model, as done with our primary backbone.

3. Results

3.1 Ablation Study

The ablation study showed that CELM enhanced classification performance of the baseline model (Table 1). With further incorporation of GRM, effects on performance depended on the graph topology. Note that we also experimented using GRM without CELM, but we found that loss did not decrease during training and the model did not learn successfully. When compared to the baseline with CELM, average AUC was slightly diminished by further including GRM-Fused or GRM-CD. The other three configurations – GRM-Separate, GRM-INV, and our proposed GRM-DC – successfully increased performance, and the largest improvements were found with GRM-DC. Of the three kinds of intermodality edges, the performance of GRM-INV was in close approximation to the average of the directed variants.

Table 1. Classification performance (AUC) with and without our CELM and different topologies of GRM.

		No CELM	+CELM	+CELM +GRM-DC	+CELM +GRM- Separate	+CELM +GRM- Fused	+CELM +GRM- INV	+CELM +GRM- CD
DIAG	BCC	93.8	94.2	92.8	95.1	94.9	96.5	93.9
	NEV	82.8	87.7	86.8	85.5	86.0	86.3	85.8
	MEL	88.3	86.2	87.6	84.2	87.5	86.7	85.5
	MISC	88.3	89.2	88.8	88.5	80.8	87.8	86.7
	SK	71.4	73.3	79.8	80.3	72.7	69.0	75.0
PN	TYP	76.0	79.7	80.1	80.6	81.1	78.9	77.3
	ATP	83.7	85.4	87.5	82.1	82.3	84.5	80.7
STR	REG	78.1	81.2	84.9	87.1	84.5	86.3	85.0
	IR	80.2	77.1	81.2	75.5	80.3	81.5	77.3
PIG	REG	79.6	80.2	81.1	77.5	80.5	78.0	80.1
	IR	79.9	80.5	83.6	83.5	70.7	85.5	85.2
RS	PRS	74.0	75.4	79.0	73.9	78.3	71.8	72.5
DaG	REG	73.9	75.4	78.6	77.8	77.7	78.5	75.3
	IR	79.9	79.6	83.1	81.3	80.0	81.3	80.9
BWV	PRS	89.6	90.0	90.8	92.6	88.2	91.8	87.9
VS	REG	78.6	82.5	80.7	79.1	85.6	85.7	85.1
	IR	74.1	81.5	75.4	82.9	78.2	80.5	79.4
Avg		80.7	82.3	83.6	82.8	81.7	83.0	82.0

Note: **Bold** in columns indicates highest performance for each class.

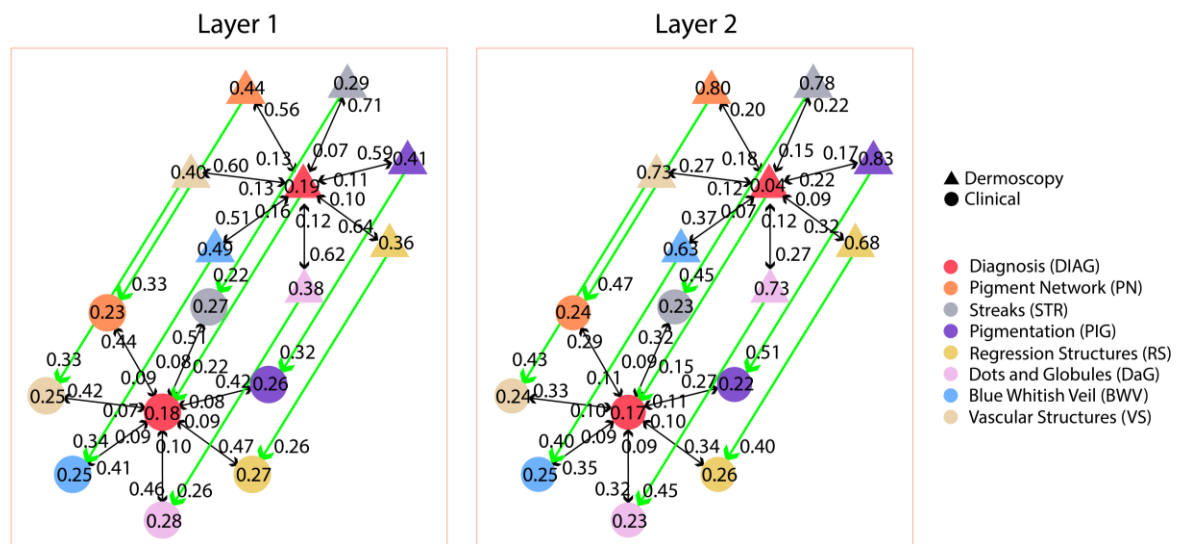


Fig. 5. Mean attention coefficients for each edge in our GIIN with CELM and GRM-DC computed on the test set, showing adaptive weighting of the contributions from the neighbours of each node. Each value corresponds to the edge with the closest arrowhead to the value. Values superimposed on each node correspond to self-attention. Coefficients sum to 1 for each node. Note: a complete list of the coefficients is in Table S2 of Supplementary Materials.

We examined the attention coefficients in the GRM to understand the strength of each relationship (Fig. 5). Notably, the average intermodality coefficients were relatively high. For both modalities in the first layer, coefficients of the edges directed from the DIAG node to the other categories were higher than corresponding self-attention coefficients. This disparity was less marked in the second layer for clinical and reversed for dermoscopy, where self-attention coefficients were substantially larger for all 7PC categories except DIAG.

The results in Table 2 indicate that overall performance on melanoma diagnosis was higher when trained with the rest of the categories and our CELM and GRM, compared to training on diagnosis alone. The average score of sensitivity, specificity, and precision for training on melanoma diagnosis was 68.0, whereas our method achieved 71.4.

Table 2. Classification performance on melanoma diagnosis of GIIN compared to training on diagnosis only without the other categories.

Method	Melanoma Diagnosis Performance			
	Sens	Spec	Prec	AUC
Melanoma Diagnosis Only	27.0	97.6	79.4	85.5
Ours	59.0	89.5	65.6	87.6

3.2 Comparison to the State-of-the-Art

We compared our GIIN with CELM and GRM-DC to the state-of-the-art methods (Table 3). Our method had an overall superior performance across precision and AUC, and was second-best across specificity.

Table 3. Classification performance of our GIIN with CELM and GRM-DC compared to the state-of-the-art.

Method	DIAG	PN	STR	PIG	RS	DaG	BWV	VS	Avg	
	MEL	ATP	IR	IR	PRS	IR	PRS	IR		
Sens	Inception-unbalanced	44.6	35.5	34.0	57.3	31.1	67.8	49.3	0.0	40.0
	Inception-balanced	55.4	41.9	50.0	67.7	62.3	66.1	65.3	10.0	52.3
	Inception-combined	61.4	48.4	51.1	59.7	66.0	62.1	77.3	13.3	54.9
	HcCNN	58.4	40.9	35.1	55.7	95.2	80.2	92.2	20.0	59.7
	Ours	59.0	77.5	67.0	39.2	21.9	70.1	69.9	3.6	51.0
Spec	Inception-unbalanced	92.2	93.7	94.0	80.1	95.5	67.4	96.6	100	89.9
	Inception-balanced	88.4	92.1	87.7	73.4	84.1	73.4	92.5	99.5	86.4
	Inception-combined	88.8	90.7	85.7	80.1	81.3	78.9	89.4	97.5	86.6
	HcCNN	88.1	92.4	90.0	86.3	41.5	71.6	65.3	98.4	79.2
	Ours	89.5	79.0	80.3	95.8	96.8	78.8	91.0	100	88.9
Prec	Inception-unbalanced	66.2	63.5	64.0	56.8	71.7	62.8	77.1	0.0	57.8
	Inception-balanced	62.2	61.9	56.0	53.8	58.9	66.9	67.1	60.0	60.9
	Inception-combined	65.3	61.6	52.7	57.8	56.5	70.5	63.0	30.8	57.3
	HcCNN	62.8	62.3	52.4	65.1	81.6	69.6	91.9	50.0	67.0
	Ours	65.6	48.4	50.4	82.3	73.5	74.9	67.4	100	70.3
AUC	Inception-unbalanced	83.2	78.6	78.3	78.1	79.9	76.4	87.0	73.4	79.4
	Inception-balanced	84.2	78.9	78.7	79.4	83.5	78.0	87.5	76.1	80.8
	Inception-combined	86.3	79.9	78.9	79.0	82.9	79.9	89.2	76.1	81.5
	HcCNN	85.6	78.3	77.6	81.3	81.9	82.6	89.8	82.7	82.5
	Ours	87.6	87.5	81.2	83.6	79.0	83.1	90.8	75.4	83.5

3.3 Application to Different Backbones

The results in Table 4 indicate that our proposed modules consistently improved the classification results across different backbones. Performance on most of the classes were

improved. Note that although the average AUC of ResNet-34 with our modules was higher than that of ResNet-50 with our modules, its overall sensitivity, specificity, and precision were inferior by a larger margin, hence we selected ResNet-50 as our main backbone network.

Table 4. Classification performance (AUC) of different backbones with or without our CELM and GRM-DC.

		MobileNet V2	MobileNet V2 (Ours)	ResNet-18	ResNet-18 (Ours)	ResNet-34	ResNet-34 (Ours)	ResNet-50	ResNet-50 (Ours)
DIAG	BCC	97.1	97.8	92.2	96.3	96.6	90.8	93.8	92.8
	NEV	86.5	85.3	84.4	88.4	88.9	86.5	82.8	86.8
	MEL	87.1	86.9	84.2	89.3	87.7	87.8	88.3	87.6
	MISC	86.7	87.2	84.6	87.7	87.3	90.0	88.3	88.8
PN	SK	85.3	80.8	70.4	81.3	81.7	82.2	71.4	79.8
	TYP	80.7	82.7	78.0	81.2	79.2	79.1	76.0	80.1
STR	ATP	77.6	79.3	79.4	79.4	79.3	80.6	83.7	87.5
	REG	87.3	88.5	83.2	88.2	87.3	84.4	78.1	84.9
PIG	IR	78.7	77.2	73.3	77.9	76.5	77.8	80.2	81.2
	REG	79.0	79.2	78.8	81.7	78.7	84.2	79.6	81.1
RS	IR	82.8	86.2	82.9	83.3	81.8	84.8	79.9	83.6
	PRS	73.0	77.8	77.7	79.2	77.7	80.4	74.0	79.0
DaG	REG	71.9	75.6	73.6	72.2	72.0	75.1	73.9	78.6
BWV	IR	76.8	79.1	80.1	78.7	77.0	83.3	79.9	83.1
	PRS	87.4	90.6	87.1	91.4	88.4	92.2	89.6	90.8
VS	REG	80.4	81.5	77.9	84.9	79.6	85.9	78.6	80.7
	IR	73.2	79.6	77.1	78.8	72.2	83.0	74.1	75.4
Avg		81.9	83.3	80.3	83.5	81.9	84.0	80.7	83.6

4. Discussion

Our main findings are that: i) the ablation study showed that our CELM and GRM improved the performance of the baseline model and the GRM-DC configuration outperformed other topological variants; ii) our proposed GIIN had superior performance when compared to the state-of-the-art methods at classifying melanoma and the 7PC categories; and iii) the benefits of our modules applied to various CNN backbones consistently.

4.1 Ablation Study

In the ablation study we showed that both our modules improved classification performance (Table 1). Though the main purpose of the CELM was to produce node embedding vectors for the categories, the module also improved the overall performance of the model due to the auxiliary learning procedure, which contributed to the individual losses for each modality, and thus provided further guidance to the intermediate features during learning. The CELM is essential for the GRM to learn successfully, as it conduces the general CNN features to specialise for each category so that the node representations of the GRM are

meaningful. Unlike previous GCN-based multilabel approaches [33-35, 37, 38], our CELM does not use pre-trained or pre-determined label embeddings. Rather, it automatically learns with the rest of the model to transform general CNN features of the skin lesion into meaningful embeddings. Furthermore, the CELM does not require further guidance other than the ground truth labels available from the dataset, such as semantic or disease knowledge.

The results for different topologies of the GRM (Table 1) demonstrated the power of our proposed structure at exploiting intercategorical and intermodal relations. The GRM-Separate variant examined the effectiveness of the star-shaped structure without blending features between modalities. The first layer of the module considers the 7PC categories for diagnosis, while each category also receives features from diagnosis. The second layer considers the more subtle relations between the 7PC categories through second-order representations. The results of GRM-Separate indicate that it is beneficial to exchange and share relevant features and relationships between categories according to the scheme of the 7PC. GRM-Fused attempted to integrate multimodal information via a concatenation of the vector embeddings of the modalities for each category. However, its poor performance suggests that this approach failed to leverage the complementary information of each modality, and that using a single modality graph structure is deleterious.

The purpose of the other three GRM variants, namely GRM-CD, GRM-INV, and GRM-DC was to investigate the optimal directionality of intermodal edges to exploit complementary multimodal features. The direction of the edges between clinical and dermoscopy determine the relative dominance of either modality, as the final outputs of the GRM comprise of ‘unmixed’ features from the more dominant modality and the ‘intermixed’ features from both modalities. As expected, prioritising clinical over dermoscopy in GRM-CD was slightly detrimental to performance (Table 1), since clinical images are inferior for lesion diagnosis than its dermoscopic counterpart [5-8]. This is also evidenced by single modality results in Table S3 of Supplementary Materials, which show weaker performance with using only clinical images compared to dermoscopy. By using intermodal edges directed from clinical to dermoscopy images, the dermoscopy features were effectively corrupted with less accurate information, thereby reducing performance. This topology is therefore not suitable to the data. The performance of GRM-INV suggests that it is approximately an average of the effects of GRM-CD and GRM-DC. The inverse edges exchange features between the modalities and result in both the detrimental and beneficial effects of prioritising the weaker and stronger modalities, respectively.

Our proposed configuration, GRM-DC, was able to leverage the benefits of intercategory relations and complementary multimodal features to improve classification, outperforming all GRM alternatives (Table 1). By using intermodal edges directed from dermoscopy to clinical, GRM-DC processes isolated dermoscopy features, and uses dermoscopy to supplement clinical features, thereby using both modalities whilst recognising that the more advanced imaging technique of dermoscopy is the more valuable modality. Moreover, we demonstrate that this configuration outperforms single modality inputs with or without CELM and GRM in Table S3 of Supplementary Materials as further evidence that our proposed module uses complementary information from both modalities.

The attention coefficients of the GATs in our GRM (Fig. 5) revealed that the contributions of dermoscopy towards clinical features were relatively large, which further reinforces the importance of the DC edges. The coefficients also imply that it is more difficult to discern each 7PC category compared to directly classifying diagnosis, as the contributions from diagnosis towards the other categories were relatively larger than their self-contributions. This suggestion is consistent with previous reports of poorer classification performance on individual skin lesion attributes (such as streaks and pigmented network) than diagnosis [47]. By leveraging intercategory relationships, our modules boosted the performance of all categories when compared to the baseline, and against directly predicting melanoma diagnosis without the other categories (Table 2).

4.2 Comparison to the State-of-the-Art

Our GIIN employed a novel strategy to combine multimodal information in comparison to the previous state-of-the-art methods. Kawahara et al. [11] combined the modalities via the simple approach of concatenation, and HcCNN [29] used a multimodal branch to combine intermediate features at various scales from both modalities. These methods, however, disregarded the qualities of each modality. Kawahara et al. [11] attempted to take advantage of the greater utility of dermoscopy at the input level with the Inception-combined approach by using different input combinations of dermoscopy with other data types. Although Inception-combined showed performance improvements, it was a suboptimal approach to better leverage dermoscopy. Furthermore, none of the previous state-of-the-art methods leveraged intercategory relations. The GIIN outperformed the state-of-the-art by exploiting both

modalities, and adaptively assigning relational importance between the categories and the modalities.

In the comparison results in Table 3, our GIIN showed some skewed behaviour for sensitivity, specificity, and precision. For example, its low sensitivity and high specificity for vascular structures (VS) indicate bias towards the negative class. We attribute this behaviour to the substantial class imbalance in the dataset [11]. There were relatively fewer examples of the positive classes, e.g., out of all 1,011 cases, there were only 71 examples of the positive (irregular, IR) class for VS, and 252 cases of melanoma. Class imbalance is a well-known issue in machine learning that can result in overfitting to the majority class. We attribute the low sensitivity of all methods to this issue. Kawahara et al. [11] attempted to alleviate such adverse effects by balancing training class examples with the Inception-balanced approach, though with mixed success (Table 3). We did not use any class-balancing techniques in our experiments as our focus was the effectiveness of our modules. Moreover, our method deems all classes as equally important, hence it may be prone to overfit to classes that are more imbalanced and bias the performance metrics. Despite this, our GIIN outperformed the state-of-the-art in terms of the mean of the average sensitivity, specificity, and precision.

4.3 Application to Different Backbones

We showed that our CELM and GRM modules could be applied to different backbone CNNs. This relates to our designing the CELM so that it could operate on a general set of CNN features from the input images and transform them into category-specific representations that are suitable for the GRM. The consistent enhancement of classification performance across the different categories for various backbones due to our modules (Table 4) demonstrates their robustness and the value of exploiting intercategory and intermodal relationships.

4.4 Future Work

More layers can be added into the GRM to investigate whether it is beneficial to include relationships that are higher than second order. Alternative topologies that emphasise additional associations between categories may be assessed depending on reported evidence. Meta-data can be incorporated into our method as a third modality to improve classification performance, as done by some previous studies [11, 24]. Different methods of meta-data

integration (e.g., concatenation or graphs), and the position of integration in the model (e.g., before, within, or after intermodal image learning) can be examined. Additionally, we will investigate class balancing techniques to potentially reduce biased performance towards the majority class. We suggest that our method may be extended to other multitask and multimodal image analysis problems such as those of PET-CT. Our CELM may also be used for datasets without appropriate pre-existing label embeddings to automatically generate such representations.

5. Conclusion

We proposed a deep learning-based method with two modules to simultaneously classify the visual categories of the 7PC and melanoma diagnosis of skin lesions in dermoscopic and clinical multimodal images. We used a graph-based relational module to exploit intercategory relationships and complementary visual features from both modalities. We also introduced a category embedding learning module to automatically produce the vector embeddings for the graph nodes of each category from general CNN features of the lesion. Our GRM and CELM modules consistently improved the classification performance of various baseline models. Our proposed GIIN outperformed state-of-the-art methods on a public skin lesion dataset.

Acknowledgements

This work was supported in part by Australian Research Council (ARC) grants (IC170100022 and DP200103748).

References

- [1] C. Garbe and U. Leiter, "Melanoma epidemiology and trends," *Clinics in Dermatology*, vol. 27, no. 1, pp. 3-9, 2009/01/01/ 2009, doi: <https://doi.org/10.1016/j.clindermatol.2008.09.001>.
- [2] W. H. Ward and J. M. Farma, "Cutaneous Melanoma: Etiology and Therapy [Internet]," 2017.
- [3] C. M. Balch *et al.*, "Final Version of 2009 AJCC Melanoma Staging and Classification," *Journal of Clinical Oncology*, vol. 27, no. 36, pp. 6199-6206, 2009/12/20 2009, doi: [10.1200/JCO.2009.23.4799](https://doi.org/10.1200/JCO.2009.23.4799).
- [4] A. Herschorn, "Dermoscopy for melanoma detection in family practice," *Canadian Family Physician*, vol. 58, no. 7, pp. 740-745, 2012.
- [5] P. Carli *et al.*, "Addition of dermoscopy to conventional naked-eye examination in melanoma screening: a randomized study," *Journal of the American Academy of Dermatology*, vol. 50, no. 5, pp. 683-689, 2004/05/01/ 2004, doi: <https://doi.org/10.1016/j.jaad.2003.09.009>.
- [6] H. Kittler, H. Pehamberger, K. Wolff, and M. Binder, "Diagnostic accuracy of dermoscopy," *The Lancet Oncology*, vol. 3, no. 3, pp. 159-165, 2002/03/01/ 2002, doi: [https://doi.org/10.1016/S1470-2045\(02\)00679-4](https://doi.org/10.1016/S1470-2045(02)00679-4).
- [7] M. E. Vestergaard, P. Macaskill, P. E. Holt, and S. W. Menzies, "Dermoscopy compared with naked eye examination for the diagnosis of primary melanoma: a meta-analysis of studies performed in a clinical setting," *British Journal of Dermatology*, vol. 159, no. 3, pp. 669-676, 2008, doi: <https://doi.org/10.1111/j.1365-2133.2008.08713.x>.
- [8] G. Argenziano and H. P. Soyer, "Dermoscopy of pigmented skin lesions – a valuable tool for early," *The Lancet Oncology*, vol. 2, no. 7, pp. 443-449, 2001/07/01/ 2001, doi: [https://doi.org/10.1016/S1470-2045\(00\)00422-8](https://doi.org/10.1016/S1470-2045(00)00422-8).
- [9] S. PUIG *et al.*, "Melanomas That Failed Dermoscopic Detection: A Combined Clinicodermoscopic Approach for Not Missing Melanoma," *Dermatologic Surgery*, vol. 33, no. 10, pp. 1262-1273, 2007, doi: <https://doi.org/10.1111/j.1524-4725.2007.33264.x>.
- [10] G. Argenziano *et al.*, "Seven-point checklist of dermoscopy revisited," *British Journal of Dermatology*, vol. 164, no. 4, pp. 785-790, 2011, doi: <https://doi.org/10.1111/j.1365-2133.2010.10194.x>.
- [11] J. Kawahara, S. Daneshvar, G. Argenziano, and G. Hamarneh, "Seven-Point Checklist and Skin Lesion Classification Using Multitask Multimodal Neural Nets," *IEEE Journal of Biomedical and Health Informatics*, vol. 23, no. 2, pp. 538-546, 2019, doi: [10.1109/JBHI.2018.2824327](https://doi.org/10.1109/JBHI.2018.2824327).
- [12] C. Carrera *et al.*, "Validity and Reliability of Dermoscopic Criteria Used to Differentiate Nevi From Melanoma: A Web-Based International Dermoscopy Society Study," *JAMA Dermatology*, vol. 152, no. 7, pp. 798-806, 2016, doi: [10.1001/jamadermatol.2016.0624](https://doi.org/10.1001/jamadermatol.2016.0624).
- [13] A. M. Forsea *et al.*, "Factors driving the use of dermoscopy in Europe: a pan-European survey," *British Journal of Dermatology*, vol. 175, no. 6, pp. 1329-1337, 2016, doi: <https://doi.org/10.1111/bjd.14895>.
- [14] G. Schaefer, B. Krawczyk, M. E. Celebi, and H. Iyatomi, "An ensemble classification approach for melanoma diagnosis," *Memetic Computing*, vol. 6, no. 4, pp. 233-240, 2014/12/01 2014, doi: [10.1007/s12293-014-0144-8](https://doi.org/10.1007/s12293-014-0144-8).
- [15] M. E. Celebi *et al.*, "A methodological approach to the classification of dermoscopy images," *Computerized Medical Imaging and Graphics*, vol. 31, no. 6, pp. 362-373, 2007/09/01/ 2007, doi: <https://doi.org/10.1016/j.compmedimag.2007.01.003>.
- [16] G. Fabbrocini *et al.*, "Automatic Diagnosis of Melanoma Based on the 7-Point Checklist," in *Computer Vision Techniques for the Diagnosis of Skin Cancer*, J. Scharcanski and M. E. Celebi Eds. Berlin, Heidelberg: Springer Berlin Heidelberg, 2014, pp. 71-107.
- [17] E. Claridge, P. N. Hall, M. Keefe, and J. P. Allen, "Shape analysis for classification of malignant melanoma," *Journal of Biomedical Engineering*, vol. 14, no. 3, pp. 229-234, 1992/05/01/ 1992, doi: [https://doi.org/10.1016/0141-5425\(92\)90057-R](https://doi.org/10.1016/0141-5425(92)90057-R).
- [18] C. Barata, M. Ruela, M. Francisco, T. Mendonça, and J. S. Marques, "Two Systems for the Detection of Melanomas in Dermoscopy Images Using Texture and Color Features," *IEEE Systems Journal*, vol. 8, no. 3, pp. 965-979, 2014, doi: [10.1109/JSYST.2013.2271540](https://doi.org/10.1109/JSYST.2013.2271540).

- [19] F. Xie, H. Fan, Y. Li, Z. Jiang, R. Meng, and A. Bovik, "Melanoma Classification on Dermoscopy Images Using a Neural Network Ensemble Model," *IEEE Transactions on Medical Imaging*, vol. 36, no. 3, pp. 849-858, 2017, doi: 10.1109/TMI.2016.2633551.
- [20] J. Zhang, Y. Xie, Y. Xia, and C. Shen, "Attention Residual Learning for Skin Lesion Classification," *IEEE Transactions on Medical Imaging*, vol. 38, no. 9, pp. 2092-2103, 2019, doi: 10.1109/TMI.2019.2893944.
- [21] L. Yu, H. Chen, Q. Dou, J. Qin, and P. Heng, "Automated Melanoma Recognition in Dermoscopy Images via Very Deep Residual Networks," *IEEE Transactions on Medical Imaging*, vol. 36, no. 4, pp. 994-1004, 2017, doi: 10.1109/TMI.2016.2642839.
- [22] J. Yang, F. Xie, H. Fan, Z. Jiang, and J. Liu, "Classification for Dermoscopy Images Using Convolutional Neural Networks Based on Region Average Pooling," *IEEE Access*, vol. 6, pp. 65130-65138, 2018, doi: 10.1109/ACCESS.2018.2877587.
- [23] Z. Yu *et al.*, "Melanoma Recognition in Dermoscopy Images via Aggregated Deep Convolutional Features," *IEEE Transactions on Biomedical Engineering*, vol. 66, no. 4, pp. 1006-1016, 2019, doi: 10.1109/TBME.2018.2866166.
- [24] N. Gessert, M. Nielsen, M. Shaikh, R. Werner, and A. Schlaefler, "Skin lesion classification using ensembles of multi-resolution EfficientNets with meta data," *MethodsX*, vol. 7, p. 100864, 2020/01/01/ 2020, doi: <https://doi.org/10.1016/j.mex.2020.100864>.
- [25] N. C. F. Codella *et al.*, "Skin lesion analysis toward melanoma detection: A challenge at the 2017 International symposium on biomedical imaging (ISBI), hosted by the international skin imaging collaboration (ISIC)," in *2018 IEEE 15th International Symposium on Biomedical Imaging (ISBI 2018)*, 4-7 April 2018 2018, pp. 168-172, doi: 10.1109/ISBI.2018.8363547.
- [26] M. E. Celebi, N. Codella, and A. Halpern, "Dermoscopy Image Analysis: Overview and Future Directions," *IEEE Journal of Biomedical and Health Informatics*, vol. 23, no. 2, pp. 474-478, 2019, doi: 10.1109/JBHI.2019.2895803.
- [27] J. Yap, W. Yolland, and P. Tschandl, "Multimodal skin lesion classification using deep learning," *Experimental Dermatology*, vol. 27, no. 11, pp. 1261-1267, 2018, doi: <https://doi.org/10.1111/exd.13777>.
- [28] Z. Ge, S. Demyanov, R. Chakravorty, A. Bowling, and R. Garnavi, "Skin Disease Recognition Using Deep Saliency Features and Multimodal Learning of Dermoscopy and Clinical Images," Cham, 2017: Springer International Publishing, in *Medical Image Computing and Computer Assisted Intervention – MICCAI 2017*, pp. 250-258.
- [29] L. Bi, D. D. Feng, M. Fulham, and J. Kim, "Multi-Label classification of multi-modality skin lesion via hyper-connected convolutional neural network," *Pattern Recognition*, vol. 107, p. 107502, 2020/11/01/ 2020, doi: <https://doi.org/10.1016/j.patcog.2020.107502>.
- [30] Z. Wu, S. Pan, F. Chen, G. Long, C. Zhang, and P. S. Yu, "A Comprehensive Survey on Graph Neural Networks," *IEEE Transactions on Neural Networks and Learning Systems*, vol. 32, no. 1, pp. 4-24, 2021, doi: 10.1109/TNNLS.2020.2978386.
- [31] T. N. Kipf and M. Welling, "Semi-Supervised Classification with Graph Convolutional Networks," 2017. [Online]. Available: <https://openreview.net/forum?id=SJU4ayYgl>.
- [32] P. Veličković, G. Cucurull, A. Casanova, A. Romero, P. Lio, and Y. Bengio, "Graph attention networks," *arXiv preprint arXiv:1710.10903*, 2017.
- [33] Z.-M. Chen, X.-S. Wei, P. Wang, and Y. Guo, "Multi-label image recognition with graph convolutional networks," in *Proceedings of the IEEE/CVF Conference on Computer Vision and Pattern Recognition*, 2019, pp. 5177-5186.
- [34] Q. Li, X. Peng, Y. Qiao, and Q. Peng, "Learning label correlations for multi-label image recognition with graph networks," *Pattern Recognition Letters*, vol. 138, pp. 378-384, 2020/10/01/ 2020, doi: <https://doi.org/10.1016/j.patrec.2020.07.040>.
- [35] Q. Meng and W. Zhang, "Multi-Label Image Classification with Attention Mechanism and Graph Convolutional Networks," presented at the Proceedings of the ACM Multimedia Asia, Beijing, China, 2019. [Online]. Available: <https://doi.org/10.1145/3338533.3366589>.
- [36] R. You, Z. Guo, L. Cui, X. Long, Y. Bao, and S. Wen, "Cross-modality attention with semantic graph embedding for multi-label classification," in *Proceedings of the AAAI Conference on Artificial Intelligence*, 2020, vol. 34, no. 07, pp. 12709-12716.

- [37] D. Hou, Z. Zhao, and S. Hu, "Multi-Label Learning With Visual-Semantic Embedded Knowledge Graph for Diagnosis of Radiology Imaging," *IEEE Access*, vol. 9, pp. 15720-15730, 2021, doi: 10.1109/ACCESS.2021.3052794.
- [38] J. Wu *et al.*, "Learning Differential Diagnosis of Skin Conditions with Co-occurrence Supervision Using Graph Convolutional Networks," Cham, 2020: Springer International Publishing, in *Medical Image Computing and Computer Assisted Intervention – MICCAI 2020*, pp. 335-344.
- [39] D.-A. Clevert, T. Unterthiner, and S. Hochreiter, "Fast and Accurate Deep Network Learning by Exponential Linear Units (ELUs)," 2016. [Online]. Available: <http://arxiv.org/abs/1511.07289>.
- [40] D. P. Kingma and J. Ba, "Adam: A Method for Stochastic Optimization," *CoRR*, vol. abs/1412.6980, 2014.
- [41] J. Deng, W. Dong, R. Socher, L. Li, L. Kai, and F.-F. Li, "ImageNet: A large-scale hierarchical image database," in *2009 IEEE Conference on Computer Vision and Pattern Recognition*, 20-25 June 2009 2009, pp. 248-255, doi: 10.1109/CVPR.2009.5206848.
- [42] K. He, X. Zhang, S. Ren, and J. Sun, "Delving Deep into Rectifiers: Surpassing Human-Level Performance on ImageNet Classification," in *2015 IEEE International Conference on Computer Vision (ICCV)*, 7-13 Dec. 2015 2015, pp. 1026-1034, doi: 10.1109/ICCV.2015.123.
- [43] X. Glorot and Y. Bengio, "Understanding the difficulty of training deep feedforward neural networks," in *Proceedings of the thirteenth international conference on artificial intelligence and statistics*, 2010, pp. 249-256.
- [44] A. Paszke *et al.*, "Pytorch: An imperative style, high-performance deep learning library," in *Advances in neural information processing systems*, 2019, pp. 8026-8037.
- [45] M. Sandler, A. Howard, M. Zhu, A. Zhmoginov, and L. Chen, "MobileNetV2: Inverted Residuals and Linear Bottlenecks," in *2018 IEEE/CVF Conference on Computer Vision and Pattern Recognition*, 18-23 June 2018 2018, pp. 4510-4520, doi: 10.1109/CVPR.2018.00474.
- [46] K. He, X. Zhang, S. Ren, and J. Sun, "Deep Residual Learning for Image Recognition," *2016 IEEE Conference on Computer Vision and Pattern Recognition (CVPR)*, pp. 770-778, 2015.
- [47] N. Codella *et al.*, "Skin lesion analysis toward melanoma detection 2018: A challenge hosted by the international skin imaging collaboration (isic)," *arXiv preprint arXiv:1902.03368*, 2019.

Supplementary Materials

Table S1. Performance (AUC) using different λ_D and λ_C

		$\lambda_D, \lambda_C = 0.1$	$\lambda_D, \lambda_C = 0.5$	$\lambda_D, \lambda_C = 1.0$
DIAG	BCC	95.9	92.8	96.2
	NEV	89.3	86.8	87.9
	MEL	88.0	87.6	87.5
	MISC	90.7	88.8	89.3
	SK	64.8	79.8	72.6
PN	TYP	82.2	80.1	83.0
	ATP	86.5	87.5	80.1
STR	REG	86.2	84.9	86.0
	IR	78.6	81.2	79.2
PIG	REG	77.5	81.1	81.5
	IR	84.3	83.6	83.5
RS	PRS	80.0	79.0	78.7
DaG	REG	76.8	78.6	77.1
	IR	81.1	83.1	79.5
BWV	PRS	89.0	90.8	91.4
VS	REG	83.1	80.7	83.4
	IR	76.3	75.4	82.8
Avg		83.0	83.6	83.5

Table S2. GRM attention coefficients

	Source Node	Destination Node	Layer 1	Layer 2
Dermoscopy	DIAG_D	PN_D	0.56	0.20
	DIAG_D	STR_D	0.71	0.22
	DIAG_D	PIG_D	0.59	0.17
	DIAG_D	RS_D	0.64	0.32
	DIAG_D	DaG_D	0.62	0.27
	DIAG_D	BWV_D	0.51	0.37
	DIAG_D	VS_D	0.60	0.27
	PN_D	DIAG_D	0.13	0.18
	STR_D	DIAG_D	0.07	0.15
	PIG_D	DIAG_D	0.11	0.22
	RS_D	DIAG_D	0.10	0.09
	DaG_D	DIAG_D	0.12	0.12
	BWV_D	DIAG_D	0.16	0.07
	VS_D	DIAG_D	0.13	0.12
Clinical	DIAG_C	PN_C	0.44	0.29
	DIAG_C	STR_C	0.51	0.32
	DIAG_C	PIG_C	0.42	0.27
	DIAG_C	RS_C	0.47	0.34
	DIAG_C	DaG_C	0.46	0.32
	DIAG_C	BWV_C	0.41	0.35
	DIAG_C	VS_C	0.42	0.33
	PN_C	DIAG_C	0.09	0.11
	STR_C	DIAG_C	0.08	0.09
	PIG_C	DIAG_C	0.08	0.11
	RS_C	DIAG_C	0.09	0.10
	DaG_C	DIAG_C	0.10	0.09
	BWV_C	DIAG_C	0.09	0.09
	VS_C	DIAG_C	0.07	0.10

Intermodal	DIAG_D	DIAG_C	0.22	0.15
	PN_D	PN_C	0.33	0.47
	STR_D	STR_C	0.22	0.45
	PIG_D	PIG_C	0.32	0.51
	RS_D	RS_C	0.26	0.40
	DaG_D	DaG_C	0.26	0.45
	BWV_D	BWV_C	0.34	0.40
	VS_D	VS_C	0.33	0.43
Self-Attention Dermoscopy	DIAG_D	DIAG_D	0.19	0.04
	PN_D	PN_D	0.44	0.80
	STR_D	STR_D	0.29	0.78
	PIG_D	PIG_D	0.41	0.83
	RS_D	RS_D	0.36	0.68
	DaG_D	DaG_D	0.38	0.73
	BWV_D	BWV_D	0.49	0.63
	VS_D	VS_D	0.40	0.73
Self-Attention Clinical	DIAG_C	DIAG_C	0.18	0.17
	PN_C	PN_C	0.23	0.24
	STR_C	STR_C	0.27	0.23
	PIG_C	PIG_C	0.26	0.22
	RS_C	RS_C	0.27	0.26
	DaG_C	DaG_C	0.28	0.23
	BWV_C	BWV_C	0.25	0.25
	VS_C	VS_C	0.25	0.24

Table S3. Performance (AUC) using single modality inputs

		Clinical	Clinical +CELM+GRM	Dermoscopy	Dermoscopy +CELM+GRM
DIAG	BCC	79.5	87.6	90.7	95.6
	NEV	80.9	82.6	82.6	86.7
	MEL	81.0	78.3	86.7	86.9
	MISC	83.0	84.4	85.9	84.2
	SK	79.7	80.0	67.1	75.9
PN	TYP	73.9	75.6	77.9	81.7
	ATP	67.3	69.2	83.0	77.6
STR	REG	77.7	77.7	78.7	88.2
	IR	70.5	69.2	79.3	78.8
PIG	REG	73.1	74.7	81.0	82.1
	IR	73.2	74.7	83.9	82.6
RS	PRS	71.7	66.2	77.0	78.6
DaG	REG	70.9	71.9	75.3	77.6
	IR	73.3	73.2	80.8	81.3
BWV	PRS	78.5	80.1	90.2	87.3
VS	REG	76.8	75.7	84.8	83.1
	IR	75.1	79.3	81.6	73.0
Avg		75.7	76.5	81.5	82.4